


 Cite this: *RSC Adv.*, 2024, **14**, 37781

High-performance H₂S gas sensor utilizing MXene/MoS₂ heterostructure synthesized via the Langmuir–Blodgett technique and chemical vapor deposition[†]

 Jae Hyuk Shin,[‡] Su Hun Jo,[‡] Hyejin Rhyu, Chanwon Park, Myung Hyun Kang,^{*} Wooseok Song, Sun Sook Lee, Jongsun Lim and Sung Myung *

In this study, we developed an H₂S gas sensor based on a MXene/MoS₂ heterostructure, using the Langmuir–Blodgett (LB) technique and chemical vapor deposition (CVD). Ti₃C₂T_x MXene nanosheets were uniformly transferred onto SiO₂/Si substrates via the LB technique, achieving near-complete coverage. Subsequently, flower-like MoS₂ was grown on the MXene-coated substrate through CVD, with vertical growth observed on the MXene layers. Our hybrid sensors exhibited a significant enhancement in gas response, with the MXene/MoS₂ heterostructure showing a response of 0.5 to H₂S – approximately five times greater than that of pristine MXene. This improvement is attributed to the formation of a heterojunction, which increases electron mobility and reduces the depletion layer, enabling more efficient gas detection. Furthermore, the sensor demonstrated excellent selectivity for H₂S over other gases, including H₂, NO₂, NH₃, NO, and VOCs. The combination of the LB technique and CVD not only enhances gas sensor performance but also offers a promising strategy for synthesizing materials for various electrochemical applications.

 Received 22nd October 2024
 Accepted 22nd November 2024

DOI: 10.1039/d4ra07555b

rsc.li/rsc-advances

Introduction

Two-dimensional (2D) materials like graphene,^{1,2} phosphorene,^{3,4} metal–organic frameworks (MOFs),^{5,6} and MXene,^{7–9} known for their high surface-to-volume ratio, large surface area, and remarkable surface activities, have garnered significant attention for various applications. Among these, MXenes, represented by the formula M_{n+1}X_nT_x (where M denotes a transition metal like Ti, V, Cr, Mo, or Ta, X represents C or N, and T stands for surface terminal groups such as –O, –F, or –OH), are particularly notable for their high electrical conductivity,¹⁰ mechanical flexibility,^{11,12} tunable band gap,^{13,14} and large surface area.¹⁵ These properties make MXenes ideal for applications in sensors,^{16,17} energy storage systems, and electronic devices.^{18,19} However, MXene-based gas sensors encounter challenges such as low response, limited functional groups, low bandgaps, and reduced mechanical stability.^{20,21} To overcome these issues, surface functionalization of MXenes has emerged as a solution, enhancing chemical reactivity, tuning electronic

properties, and improving structural stability, unlocking the potential of MXenes in various technologies.^{22–24}

One approach to address these challenges is to incorporate materials like TMDs, metal oxides, and polymers onto the MXene surface. Recently, 2D semiconducting transition metal dichalcogenides (TMDs), with chemical formulas such as MX₂ (M = Mo, W; X = S, Se), have attracted great attention for their unique structural features and outstanding properties.^{25–27} In practice, NH₃ gas sensors using WS₂ synthesized through sulfurization via CVD have been studied, as well as H₂S gas sensors based on MoS₂ synthesized with rGO using the hydrothermal method.^{28,29} Among them, MoS₂ stands out, with a tunable bandgap that ranges from 1.8 eV in monolayer form to ~1.2 eV in bulk, making it suitable for a wide range of applications. MoS₂ also offers excellent carrier mobility, high surface area, mechanical strength, and flexibility due to the covalent bonding of Mo and S, making it highly desirable for sensors, photocatalysis, and energy storage.^{30,31} In particular, properties of MoS₂ make it ideal for various-type sensor applications when combined with MXene in heterostructures.^{32–34} Recent studies have successfully fabricated MXene/MoS₂ heterostructures using methods such as hydrothermal synthesis and sonication, applying them to reactive gas sensors.^{35,36}

In this study, we utilized the LB technique to deposit a monolayer of uniform Ti₃C₂T_x MXene nanosheets onto a substrate, optimizing their arrangement by controlling

Thin Film Materials Research Group, Korea Research Institute of Chemical Technology, Daejeon 34114, South Korea. E-mail: mh0827@kRICT.re.kr; msung@kRICT.re.kr

† Electronic supplementary information (ESI) available. See DOI: <https://doi.org/10.1039/d4ra07555b>

‡ Equally contributed.



packing density. For densely packed MXene layers, defects such as overlapping nanosheets and artificial grain boundaries were observed. We then synthesized MoS_2 with unique structures on the MXene-coated substrate. As a result, flower-like MoS_2 structures grew on the MXene substrate, providing the MXene/ MoS_2 structure with more binding sites, which was expected to enhance gas reactivity. The structure demonstrated excellent sensing performance particularly showing high sensitivity to H_2S among various gases. This heterostructure improves surface-to-volume ratios and enhances post-reaction recovery, addressing key limitations of conventional 2D materials in gas-sensing applications.

Experimental

Synthesis of MXene nanosheets

1 g of MAX (Ti_3AlC_2) powder was dispersed in a mixed solvent composed of HF, HCl, and deionized water in a 3:6:1 volume ratio for 24 hours. To separate the supernatant and obtain $\text{Ti}_3\text{C}_2\text{T}_x$ nanosheets, the solution was adjusted to a pH of 6.0 and centrifuged at 12 000 rpm for 10 minutes. Subsequently, 50 mL of the $\text{Ti}_3\text{C}_2\text{T}_x$ solution was allowed to react with 10 mL of LiCl solution for 4 hours. The intercalated $\text{Ti}_3\text{C}_2\text{T}_x$ solution was then centrifuged with 150 mL of deionized water at 3000 rpm for 10 minutes to obtain the supernatant.

LB method for transfer of MXene

The MXene film was deposited *via* the LB method using the extracted suspension. The dispersed solution was poured into an LB trough (KSV Minimicro, Teflon trough with an active trough surface area of 273 cm^2 , that is, $L 364 \times W 75 \times H 4 \text{ mm}^3$, and a dipping well of $L 20 \times W 56 \times H 60 \text{ mm}^3$; trough volume: 110 cm^3) until the surface pressure reached 20 N mm^{-2} . The compression process was started using a compression speed of 3 mm min^{-1} and continued until the surface pressure was reached at $30\text{--}35 \text{ mN m}^{-1}$. The film floating at the interface was transferred onto a SiO_2/Si substrate once using the vertical dipping method at a transfer rate of 1.0 mm min^{-1} to adjust the thickness of MXene layers.

Synthesis of MXene/ MoS_2 film

The MXene film was initially deposited onto a SiO_2/Si substrate using the LB method. MoS_2 layers were subsequently grown in a furnace equipped with a 1-inch quartz tube. In this process, a mixture of MoO_3 powder (Sigma-Aldrich, 99.97%, 25 g) was placed in an alumina boat positioned at the front of the furnace's heating zone, while the SiO_2/Si substrates were placed at the center of the heating zone. The reaction was initiated using an Ar/ H_2S gas mixture (Seoul specialty gas, H_2S 10%, 47 L), along with Ar (99.99%, 47 L) and H_2 (99.99%, 47 L) as carrier gases. The furnace was first thermally annealed at $700 \text{ }^\circ\text{C}$ with a heating rate of $13.5 \text{ }^\circ\text{C}$ per minute for 50 minutes under a flow of 50 sccm of Ar. MoS_2 films were then grown on the MXene-coated substrate at $700 \text{ }^\circ\text{C}$ for 30 minutes using a layer-by-layer growth mode. During this synthesis, the flow rates of H_2 , Ar, and Ar/ H_2S gases were maintained at 50, 50, and 25 sccm, respectively. The reaction

pressure within the two-zone furnace was maintained at approximately 0.3 torr. After synthesis, the MXene/ MoS_2 structure on the substrate was allowed to cool naturally by turning off the heat source, with the material cooling in ambient air.

Characterizations of the MXene/ MoS_2

The morphologies of the synthesized MXene/ MoS_2 were analyzed by field-emission scanning electron microscopy (FE-SEM, Hitachi, S-4700) and energy-dispersive X-ray spectroscopy (EDS). The crystallinity of MXene/ MoS_2 crystals was investigated through transition electron microscopy (TEM, Titan Cube G2 60-300, FEI Company). Additionally, Raman spectroscopy (inVia Raman spectrometer, Renishaw) was employed to confirm the composition of the hybrid layer, using a 532 nm excitation wavelength laser.

Fabrication of gas sensors based MXene/ MoS_2

To measure the gas responses of the device, Cr and Au (Cr 3 nm, Au 70 nm) were deposited as electrodes on the substrate using thermal evaporation. To evaluate the resistance change of the sensor, H_2 , H_2S , NO, NO_2 , NH_3 , ethanol, and acetone gases were individually injected into the sensing chamber. The sensor was placed 2 cm away from the gas inlet, and measurements were conducted at a temperature of $250 \text{ }^\circ\text{C}$ with a relative humidity of 25%. The electrical characteristics of the sensor were recorded using a semiconductor parameter analyzer (Keithley-4200, Keithley Instruments, USA).

Results and discussion

To synthesize the MXene/ MoS_2 layer, MXene nanosheets were prepared following previously work.³⁷ Briefly, HF combined with hydrochloric acid HCl was used for etching, followed by delamination using LiCl, a widely recognized method for producing high-quality MXene *via* alkaline cation intercalation and subsequent delamination (Fig. 1a). This process separated the accordion-like stacked MXene layers into individual nanosheets, enabling 2D epitaxial growth through van der Waals interactions. The resulting thin MXene nanosheets were then coated onto a substrate using the LB technique (Fig. 1b). The LB technique is commonly employed to fabricate ultrathin films from nanoparticles, nanowires, and nanosheets, offering high structural organization and reliability.^{38,39} The LB method stands out for producing monolayer films. This method is particularly effective for producing monolayer films, where molecules or particles are first dissolved in a volatile, water-immiscible solvent and spread onto the water surface. As the solvent evaporates, a monolayer forms and is compressed using movable barriers to control material density. For this study, the compression speed was set at a slow 3 mm min^{-1} , maintaining the surface pressure at $30\text{--}35 \text{ mN m}^{-1}$ to minimize overlap on the surface. Two successive transfers of MXene nanosheets were carried out to ensure uniform coverage. The sheet resistance of MXene and MXene/ MoS_2 was measured, revealing that MXene nanosheets exhibited a sheet resistance of several hundred ohms/sq. after a single transfer onto an SiO_2/Si substrate using



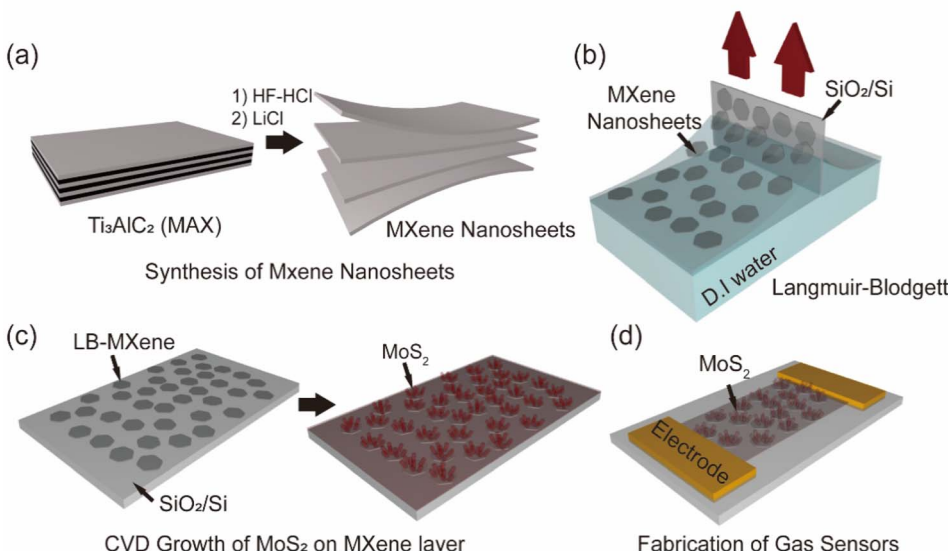


Fig. 1 Schematic illustration of the synthesis of MXene/MoS₂. (a) Preparation of MXene nanosheets from MAX phase, (b) thin layer formation of MXene on SiO₂/Si substrate using LB technique, (c) Growth of MoS₂ on LB-MXene, and (d) fabrication of LB-MXene/MoS₂ based gas sensor.

the LB technique (Fig S1†). The sheet resistance was found to decrease with ν . A total of two MXene nanosheet transfers were performed using this technique. Fig. 1c illustrates the uniform synthesis of MoS₂ on the MXene nanosheets *via* CVD. During synthesis, the inert Ar and H₂ atmosphere effectively minimized the oxidation of MXene nanosheets to TiO₂, although partial oxidation of Ti₃C₂T_x was unavoidable during the LB process. Finally, as shown in Fig. 1d, a resistive-type gas sensor was fabricated by depositing Au and Cr electrodes onto the SiO₂/Si substrate with the synthesized MXene/MoS₂ layer using thermal

evaporation. Our novel method fabricates thin and uniform MXene sheets, followed by the synthesis of flower-shaped MoS₂ *via* CVD, which is not only uniform to the MXene nanosheets but also offer more gas adsorption sites than either individual material, and is expected to be applied as a gas sensor.

To analyze the morphology of the MoS₂ on MXene layers, we performed FE-SEM were checked at each stage of the synthesis of the composite material. As shown in Fig. 2a, the image depicts the substrate with MXene nanosheets transferred *via* the LB method. Although some gaps are present, the MXene

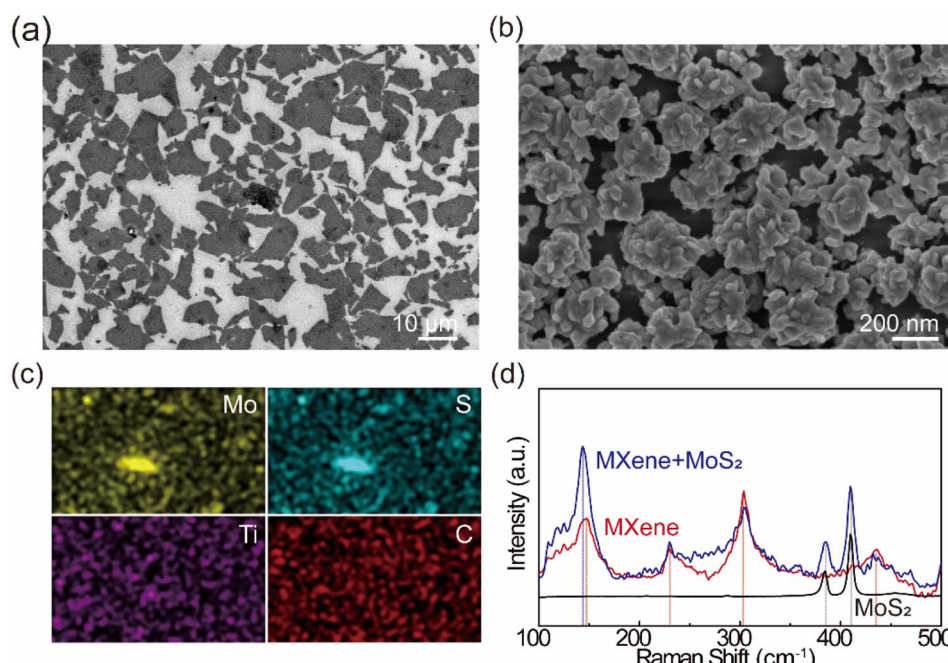


Fig. 2 Morphology and structural analysis of the MXene/MoS₂. SEM image of (a) the LB-MXene nanosheets onto a SiO₂/Si substrate, (b) the synthesized MoS₂ on LB-MXene, (c) EDS mapping images of MXene/MoS₂, (d) Raman spectrum of MoS₂, MXene, and MXene/MoS₂.



nanosheets transferred onto the substrate formed a monolayer without overlapping, consistent with the characteristics of the LB technique. As the MXene nanosheets were transferred onto the SiO_2/Si substrate using the LB method, they formed a very thin layer, allowing the Si peak at 69.26° to be observed clearly (Fig. S2†). This confirmed that the LB technique successfully transferred the MXene nanosheets onto the substrate. Subsequently, MoS_2 was grown using a CVD process with MoO_3 powder and H_2S gas. When we investigated the roughness of the MoS_2 synthesized on LB-MXene (Fig. S3†), we found that the MXene nanosheets were not laying in the same orientation, resulting in the synthesis of MoS_2 on MXene with random morphology and roughness. As shown in Fig. 2b, MoS_2 grew uniformly across the substrate, with nanoflower-like structures vertically grown on top of the MXene nanosheets. When MoS_2 was grown on the substrate with transferred MXene nanosheets, MoS_2 grew across the entire surface, but particularly on the MXene nanosheets, it grew vertically, forming a nanoflower-like morphology. This provided more adsorption sites compared to pristine MXene, suggesting better performance as a gas sensor. The results (Fig. 2c) indicated the significant elements for the MXene/ MoS_2 (Ti, C, Mo, and S). It was confirmed that each of the main elements is uniformly distributed. As shown in Fig. 2d, the characteristic peaks of pristine MoS_2 , the E_{2g} peak at 384.66 cm^{-1} and the A_{1g} peak at 409.76 cm^{-1} , were also observed after the synthesis of MXene. The distance between the E_{2g} peak and the A_{1g} peak of MoS_2 was 25.12 cm^{-1} , indicating the growth of multilayer MoS_2 . Additionally, the peak observed at 147.55 cm^{-1} in pristine MXene shifted by approximately 3.5 cm^{-1} to 143.85 cm^{-1} after the growth of MoS_2 , with a corresponding increase in intensity. This is a typical E_{2g} peak of TiO_2 , and it is presumed that, as a portion of MXene was oxidized into MXene-derived TiO_2 during the growth of MoS_2 , stress or defects generated during the oxidation process affected the local structure of the material, causing a shift in the Raman peak and an increase in intensity due to improved crystallinity. Raman analysis (Fig. S4†) was conducted at eight randomly designated sites, revealing the presence of both MoS_2 and MXene peaks at each site. This confirmed not only the uniform distribution of the main elements but also consistent chemical bonding between MoS_2 and MXene. Therefore, we present an approach to synthesize homogeneous MoS_2 using a simple method.

To evaluate the gas sensing properties of the MXene/ MoS_2 -based sensor, we compared the gas reactivity of pristine MoS_2 with that of the MXene/ MoS_2 heterostructure (Fig. 3a and S5†).

The gas response of the sensor is represented by R , and the corresponding reaction equation is as follows:

$$\text{Gas response } (R) = R_a/R_g \text{ or } R_g/R_a$$

Both MXene and MoS_2 are generally recognized as n-type materials, which makes them well-suited for detecting oxidative gases. A notable improvement in reactivity towards reducing gases, such as H_2S and H_2 , was observed with the formation of the MXene/ MoS_2 heterostructure. Furthermore,

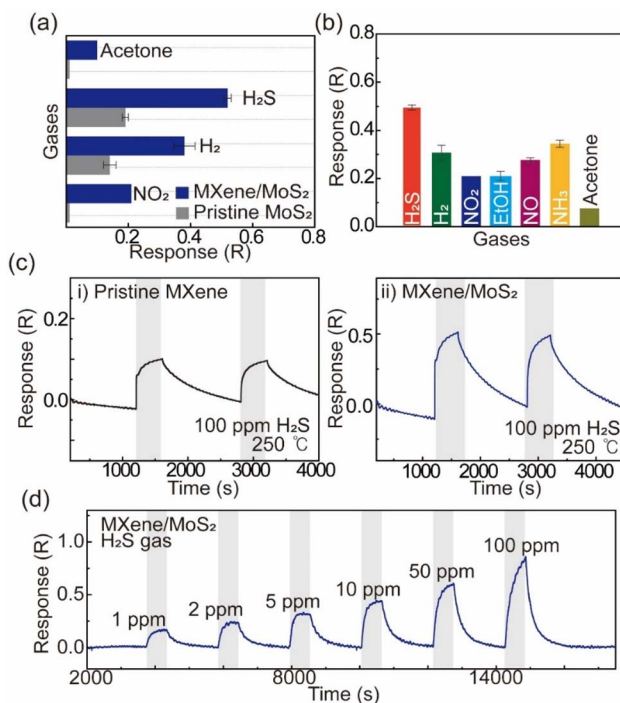


Fig. 3 Gas sensing properties of the MXene/ MoS_2 gas sensor. (a) Comparisons of response value between pristine MXene and MXene/ MoS_2 about various gases. The gas responses of MXene/ MoS_2 at various gases (H_2S , H_2 , NO_2 , ethanol, NO , NH_3 , and acetone) at 100 ppm, (b) the gas responses of MXene/ MoS_2 at various gases at 100 ppm, (c) the dynamic response curve to H_2S gas response of (i) the pristine MXene and (ii) the MXene/ MoS_2 based gas sensor, and (d) H_2S Gas responses of the MXene/ MoS_2 based gas sensor at various concentration of H_2S (100 ppm to 1 ppm). All gas responses were measured in a dry atmosphere.

the sensitivity to oxidizing gases, particularly NO_2 , was significantly enhanced, suggesting that the n-type/n-type heterostructure is highly effective in improving gas sensing performance. Fig. 3b and S6 in ESI† presents the response of the MXene/ MoS_2 gas sensor to various gases (H_2S , H_2 , NO_2 , ethanol, NO , NH_3 , and acetone), with the highest response observed for H_2S . Fig. 3c shows the dynamic response curve for 100 ppm of H_2S , where the MXene/ MoS_2 heterostructure exhibits approximately a five-fold increase in sensitivity compared to the pristine MXene sensor. The slightly lower gas response in the second cycle is related to the gas desorption time on the surface of the MXene/ MoS_2 . We also conducted a follow-up test on the MXene/ MoS_2 device a week later, which demonstrated a stable gas response of approximately 0.50 for H_2S , confirming its long-term stability (Fig. S7†). Furthermore, as shown in Fig. 3d, the MXene/ MoS_2 gas sensor demonstrated a notable gas response of 0.17 even at a low concentration of 1 ppm of H_2S . Based on the limit of detection (LOD) definition defined by the International Union of Pure and Applied Chemistry (IUPAC), the gas sensor demonstrated the ability to detect H_2S at concentrations as low as 0.87 ppb, according to the calculated LOD as shown in Fig. S8.† These results suggest that the uniform vertical growth of MoS_2 on MXene contributes to the enhancement of gas sensing performance by providing more adsorption sites,



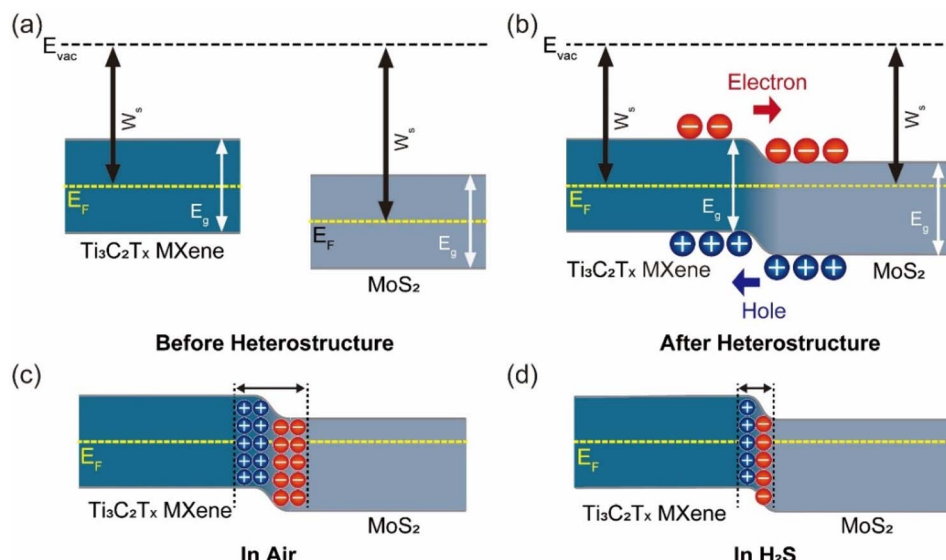
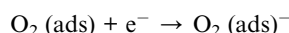
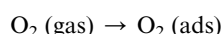


Fig. 4 Band diagram of chemi-resistive gas sensor based on MXene/ MoS_2 layer. Band diagrams before (a) and after (b) forming the heterostructure between MXene and MoS_2 . Band diagram under air (c) and H_2S (d) injection.

improving gas sensing performance. Therefore, we propose that this method offers a promising solution to overcome the limitations in surface functionalization commonly faced by materials such as MXene and MoS_2 .

To understand the enhanced gas response toward H_2S compared to pristine MXene, we studied the mechanism of the MXene/ MoS_2 heterostructure. As illustrated in Fig. 4a and b, when MXene and MoS_2 exist independently, each material maintains its respective Fermi level, when a heterojunction is formed between MXene and MoS_2 , band bending occurs due to the alignment of the Fermi levels of the two materials. This results in the bending of the conduction band and valence band. When the MXene/ MoS_2 heterojunction is exposed to oxygen, oxygen ions are adsorbed on the surface, forming a depletion layer (Fig. 4c). Upon the introduction of H_2S , interactions between H_2S molecules and O_2 (ads) cause electrons to transfer to the conduction band of MoS_2 , reducing the number of holes in MXene (Fig. 4d). This process leads to the re-ionization of electron–hole pairs, which increases the number of free electrons, further reducing the width of the depletion layer. Consequently, this leads to a decrease in resistance, which directly reflects the enhanced responsiveness of the resistive gas sensor.

The reaction equations related to this are as follows:



Also, we expected that the MXene-derived TiO_2 provides more active sites compared to pristine MXene, facilitating the adsorption of more gas molecules on the surface, which in turn

contributes to the improved gas sensing performance.^{40,41} This synergy between MXene and MoS_2 enhances the overall gas sensing mechanism by promoting more efficient electron transfer and gas molecule interaction at the heterojunction.

Conclusion

In conclusion, we successfully achieved uniform transfer of MXene nanosheets onto a substrate using the LB technique. Following this, flower-like MoS_2 was uniformly grown on the MXene-coated substrate using CVD, with selective vertical growth observed on the MXene nanosheets. In terms of gas-sensing performance, pristine MXene exhibited a gas response of 0.1 to H_2S , whereas the MXene/ MoS_2 heterostructure showed a markedly enhanced response of 0.5, representing approximately five times greater sensitivity. This improvement is attributed to the formation of a heterojunction between MXene and MoS_2 , which reduced the depletion layer and expanded the region for free movement of electrons and holes. The enhanced electron mobility facilitated more efficient gas detection, while the increased conductivity addressed the slow resistance recovery typically seen in hydrogen-based gas sensors. Additionally, the sensor exhibited the highest gas response to H_2S among various gases tested. Thus, this novel synthesis approach, combining the uniform transfer of MXene *via* the LB technique and the growth of MoS_2 through CVD, not only enables the simple preparation of heterostructured materials but also enhances the gas-sensing performance by creating an n-type/n-type composite, which improves the detection of the target gas.

Data availability

The data supporting this article have been included as part of the ESI.[†]



Author contributions

Jae Hyuk Shin: investigation, data curation, writing – original draft. Su Hun Jo: investigation, data curation, writing – editing. Hyejin Rhyu: investigation. Chanwon Park: data curation. Myung Hyun Kang: data curation, supervision, writing – review & editing. Wooseok Song: validation. Sun Sook Lee: validation. Jongsun Lim: validation. Sung Myung: conceptualization, supervision, writing – review & editing.

Conflicts of interest

There are no conflicts to declare.

Acknowledgements

This research was supported by the Nanomaterial Technology Development Program through the National Research Foundation of Korea (NRF) funded by the Ministry of Science and ICT (NRF-2021M3H4A3A02086431). We also acknowledge the financial support from the Development of Smart Chemical Materials for IoT Devices Project (KS2421-10) through the Korea Research Institute of Chemical Technology.

References

- 1 S. Gupta Chatterjee, S. Chatterjee, A. K. Ray and A. K. Chakraborty, *Sens. Actuators, B*, 2015, **221**, 1170–1181.
- 2 C. Chung, Y.-K. Kim, D. Shin, S.-R. Ryoo, B. H. Hong and D.-H. Min, *Acc. Chem. Res.*, 2013, **46**, 2211–2224.
- 3 M. Batmunkh, M. Bat-Erdene and J. G. Shapter, *Adv. Mater.*, 2016, **28**, 8586–8617.
- 4 R. Irshad, K. Tahir, B. Li, Z. Sher, J. Ali and S. Nazir, *J. Ind. Eng. Chem.*, 2018, **64**, 60–69.
- 5 X. Wu, X. Tian, W. Zhang, X. Peng, S. Zhou, P. J. S. Buenconsejo, Y. Li, S. Xiao, J. Tao, M. Zhang and H. Yuan, *Angew. Chem., Int. Ed.*, 2024, e202410411.
- 6 T. Lee, J.-O. Kim, C. Park, H. Kim, M. Kim, H. Park, I. Kim, J. Ko, K. Pak, S. Q. Choi, I.-D. Kim and S. Park, *Adv. Mater.*, 2022, **34**, 2107696.
- 7 Q. Jiang, Y. Lei, H. Liang, K. Xi, C. Xia and H. N. Alshareef, *Energy Storage Mater.*, 2020, **27**, 78–95.
- 8 X. Zhan, C. Si, J. Zhou and Z. Sun, *Nanoscale Horiz.*, 2020, **5**, 235–258.
- 9 S. Mehdi Aghaei, A. Aasi and B. Panchapakesan, *ACS Omega*, 2021, **6**, 2450–2461.
- 10 J. Liu, Z. Liu, H.-B. Zhang, W. Chen, Z. Zhao, Q.-W. Wang and Z.-Z. Yu, *Adv. Electron. Mater.*, 2020, **6**, 1901094.
- 11 C. Ma, M.-G. Ma, C. Si, X.-X. Ji and P. Wan, *Adv. Funct. Mater.*, 2021, **31**, 2009524.
- 12 W. Yang, J.-J. Liu, L.-L. Wang, W. Wang, A. C. Y. Yuen, S. Peng, B. Yu, H.-D. Lu, G. H. Yeoh and C.-H. Wang, *Composites, Part B*, 2020, **188**, 107875.
- 13 Y. Zhang, W. Xia, Y. Wu and P. Zhang, *Nanoscale*, 2019, **11**, 3993–4000.
- 14 Z. Ma, Z. Hu, X. Zhao, Q. Tang, D. Wu, Z. Zhou and L. Zhang, *J. Phys. Chem. C*, 2014, **118**, 5593–5599.
- 15 L. Zhang, W. Song, H. Liu, H. Ding, Y. Yan and R. Chen, *Processes*, 2022, **10**, 1744.
- 16 S. J. Kim, H.-J. Koh, C. E. Ren, O. Kwon, K. Maleski, S.-Y. Cho, B. Anasori, C.-K. Kim, Y.-K. Choi, J. Kim, Y. Gogotsi and H.-T. Jung, *ACS Nano*, 2018, **12**, 986–993.
- 17 G. Hang, X. Wang, J. Zhang, Y. Wei, S. He, H. Wang and Z. Liu, *ACS Appl. Nano Mater.*, 2022, **5**, 14191–14208.
- 18 X. Zhang, Z. Zhang and Z. Zhou, *J. Energy Chem.*, 2018, **27**, 73–85.
- 19 R. E. Ustad, S. S. Kundale, K. A. Rokade, S. L. Patil, V. D. Chavan, K. D. Kadam, H. S. Patil, S. P. Patil, R. K. Kamat, D.-k. Kim and T. D. Dongale, *Nanoscale*, 2023, **15**, 9891–9926.
- 20 H.-F. Zhang, J.-Y. Xuan, Q. Zhang, M.-L. Sun, F.-C. Jia, X.-M. Wang, G.-C. Yin and S.-Y. Lu, *Rare Met.*, 2022, **41**, 3976–3999.
- 21 Q. Xia, Y. Fan, S. Li, A. Zhou, N. Shinde and R. S. Mane, *Diam. Relat. Mater.*, 2023, **131**, 109557.
- 22 D. Han, Z. Liu, L. Liu, D. Li, Y. Chen, H. Wang, L. Zhao, W. Wang and S. Sang, *Sens. Actuators, B*, 2023, **393**, 134319.
- 23 H. Yu, L. Dai, Y. Liu, Y. Zhou, P. Fan, J. Luo and A. Zhong, *J. Alloys Compd.*, 2023, **962**, 171170.
- 24 B. Sun, H. Lv, Z. Liu, J. Wang, X. Bai, Y. Zhang, J. Chen, K. Kan and K. Shi, *J. Mater. Chem. A*, 2021, **9**, 6335–6344.
- 25 S. Sardana, A. K. Debnath, D. K. Aswal and A. Mahajan, *Sens. Actuators, B*, 2023, **394**, 134352.
- 26 Y. Xia, S. He, J. Wang, L. Zhou, J. Wang and S. Komarneni, *Chem. Commun.*, 2021, **57**, 9136–9139.
- 27 S. H. Hosseini-Shokouh, J. Zhou, E. Berger, Z.-P. Lv, X. Hong, V. Virtanen, K. Kordas and H.-P. Komsa, *ACS Appl. Mater. Interfaces*, 2023, **15**, 7063–7073.
- 28 S. B. Malik, F. E. Annanouch, R. D'Souza, C. Bittencourt, M. Todorović and E. Llobet, *ACS Appl. Mater. Interfaces*, 2024, **16**, 48585–48597.
- 29 G. M. Hingangavkar, S. A. Kadam, Y.-R. Ma, M. Selvaraj, R. N. Mulik and V. B. Patil, *Sens. Actuators, B*, 2024, **399**, 134843.
- 30 O. Samy, S. Zeng, M. D. Birowosuto and A. El Moutaouakil, *Crystals*, 2021, **11**, 355.
- 31 U. Krishnan, M. Kaur, K. Singh, M. Kumar and A. Kumar, *Superlattices Microstruct.*, 2019, **128**, 274–297.
- 32 F. K. Perkins, A. L. Friedman, E. Cobas, P. M. Campbell, G. G. Jernigan and B. T. Jonker, *Nano Lett.*, 2013, **13**, 668–673.
- 33 D. Xu, L. Duan, S. Yan, Y. Wang, K. Cao, W. Wang, H. Xu, Y. Wang, L. Hu and L. Gao, *Micromachines*, 2022, **13**, 660.
- 34 J. Lee, P. Dak, Y. Lee, H. Park, W. Choi, M. A. Alam and S. Kim, *Sci. Rep.*, 2014, **4**, 7352.
- 35 L. Lu, M. Liu, Q. Sui, C. Zhang, Y. Zou, F. Xu, L. Sun and C. Xiang, *Mater. Today Commun.*, 2023, **35**, 106239.
- 36 S. Kim, H. Shin, J. Lee, C. Park, Y. Ahn, H.-J. Cho, S. Yuk, J. Kim, D. Lee and I.-D. Kim, *ACS Nano*, 2023, **17**, 19387–19397.
- 37 H. Rhyu, S. Jang, J. H. Shin, M. H. Kang, W. Song, S. S. Lee, J. Lim and S. Myung, *ACS Appl. Mater. Interfaces*, 2024, **16**, 28808–28817.



38 M. Bodik, M. Demydenko, T. Shabelnyk, Y. Halahovets, M. Kotlar, D. Kostiuk, A. Shaji, A. Brunova, P. Veis, M. Jergel, E. Majkova and P. Siffalovic, *J. Phys. Chem. C*, 2020, **124**, 15856–15861.

39 L. J. Cote, F. Kim and J. Huang, *J. Am. Chem. Soc.*, 2009, **131**, 1043–1049.

40 X. Tian, L. Yao, X. Cui, R. Zhao, T. Chen, X. Xiao and Y. Wang, *J. Mater. Chem. A*, 2022, **10**, 5505–5519.

41 H.-P. Li, J. Wen, S.-M. Ding, J.-B. Ding, Z.-H. Song, C. Zhang, Z. Ge, X. Liu, R.-Z. Zhao and F.-C. Li, *Nano Mater. Sci.*, 2023, **5**, 421–428.

